ACS APPLIED ENERGY MATERIALS

www.acsaem.org Article

Decoding Morphological Control in Isomeric Non-Fullerene Acceptor−Polymer Blends for Organic Solar Cells

Ram Sewak, Krishna Singh, and Anirban Mondal*

Cite This: https://doi.org/10.1021/acsaem.5c01643 Read Online

ACCESS | Metrics & More | Article Recommendations | Supporting Information

ABSTRACT: Optimizing organic solar cells necessitates a fundamental understanding of how noncovalent interactions influence the miscibility and stability of nonfullerene acceptor (NFA)−polymer blends. In this study, we employ molecular simulations combined with data-driven analysis to elucidate the impact of regioisomerism on phase morphology in Y-series fused-ring NFAs. Specifically, we compare a C-shaped isomer (CF) and an S-shaped isomer (SF) when blended with the donor polymer D18. Our findings reveal that the CF blend exhibits superior miscibility, attributed to stronger van der Waals interactions—including hydrogen bonding and interactions involving sulfur and electronegative atoms—as well as enhanced dipole−dipole interactions. These interactions collectively contribute to greater blend stability, as supported by noncovalent interactions and energy decomposition analyses. Furthermore, *k*-means clustering of molecular dynamics trajectories was employed to assess miscibility, corroborating the superior miscibility of the CF blend, while the SF blend demonstrated phase segregation. Voronoi tessellation analysis provides a geometric perspective, linking uniform molecular packing in the CF blend to minimal void spaces, whereas the SF blend exhibits structural heterogeneity and aspherical cavities. These insights establish a direct connection among isomeric configuration, intermolecular forces, and blend morphology, offering a predictive framework for designing high-performance organic solar cells.

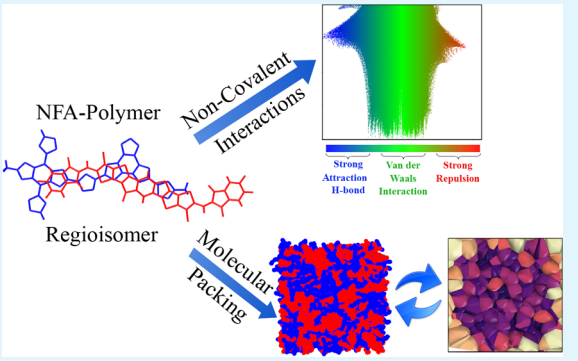

KEYWORDS: *regioisomerism, molecular packing, phase formation, organic solar cell, multiscale simulations*

1. INTRODUCTION

Organic solar cells (OSCs) have witnessed rapid advancements, driven by innovative materials and intelligent device engineering.[1−7] A key factor behind this progress is the development of fused-ring nonfullerene acceptors (FRNFAs), particularly the Y-series acceptors.[7−12] These acceptors have been instrumental in enabling multiple charge transport channels and enhances the power conversion efficiency (PCE) of OSCs by strong and broad near-infrared light absorption through the incorporation of electron-deficient cores.[13−15] To further improve photovoltaic efficiency, it is essential to establish clear correlations between molecular structure, morphology, macroscopic properties, and overall device performance.[16−19] Achieving this requires the precise tailoring of nonfullerene acceptors to facilitate systematic investigations into their structure−property relationships.

Among the various factors influencing OSC efficiency, molecular geometry plays a pivotal role in determining both material properties and device performance.[20,21] Recent studies have emphasized the significance of isomeric structures, particularly in acceptor−donor−acceptor (A-D-A) conjugated frameworks.[22] In this context, Huang and coauthors synthesized two isomeric Y-series FRNFAs—one with a C-shaped (CF) geometry and the other with an S-shaped (SF) geometry—to explore how these distinct structural configurations impact OSC performance. Their findings revealed that while optical and electrochemical properties remained largely unchanged between the isomers, substantial differences emerged in molecular packing and device efficiency. Notably, the C-shaped acceptor exhibited superior performance, yielding a remarkable power conversion efficiency of 17.0%, significantly outperforming its S-shaped counterpart. This improvement was primarily attributed to reduced voltage loss and distinct packing characteristics, even in the absence of the conventional three-dimensional stacking network typically observed in C-shaped Y-series FRNFAs.[22] Moreover, the study found that the SF:D18 (donor polymer) blend exhibited a significantly higher Flory−Huggins interaction parameter (χ = 2.70 K) compared to the CF:D18 blend (χ = 0.57 K), indicating poor miscibility between SF and the donor polymer D18. This poor miscibility led to extensive phase separation, as

Received: May 30, 2025
Revised: July 9, 2025
Accepted: July 16, 2025

corroborated by atomic force microscopy (AFM) and transmission electron microscopy (TEM) results.

While these experimental observations suggest a crucial role for molecular geometry in OSC performance, several fundamental questions remain unanswered. What types of interactions govern the morphological differences between the CF:D18 and SF:D18 blends? What are the key factors enhancing miscibility in the active layer? Addressing these questions requires a deeper understanding of the molecular-level interactions that influence blend morphology and charge transport.

To bridge this gap, we conducted comprehensive theoretical studies employing molecular dynamics (MD) simulations, density functional theory (DFT) calculations, and energy decomposition analysis. These approaches allowed us to systematically investigate the microscopic interactions between C- or S-shaped NFAs and the D18 donor polymer within the OSC active layer. Our simulation results revealed significant differences in radial distribution functions (RDFs) for key molecular pairs, highlighting interactions such as CH-π interactions, hydrogen bonding, and other noncovalent interactions involving sulfur and electronegative atoms (oxygen, fluorine, and nitrogen). Notably, C-shaped NFAs exhibited stronger interactions with the donor polymer, a finding further supported by energy decomposition analysis. To gain further insight into the morphological characteristics of these blends, we employed a *k*-means clustering algorithm to analyze cluster size distributions. Our results demonstrated that C-shaped NFAs form smaller, well-dispersed clusters, promoting better mixing with the donor polymer. In contrast, S-shaped NFAs tended to aggregate into larger clusters, leading to greater phase separation. These trends were further validated by Voronoi analysis, reinforcing the conclusion that C-shaped NFAs enhance miscibility and, consequently, OSC efficiency.

In this manuscript, we present a detailed analysis of our molecular simulations, providing fundamental insights into the superior performance of C-shaped FRNFAs in OSCs. Our findings not only corroborate experimental observations but also offer a deeper understanding of how molecular geometry influences intermolecular interactions and blend morphology. By establishing these structure–property relationships, this study contributes to the rational design of next-generation OSC materials and advances the optimization of high-efficiency organic photovoltaic devices.

2. METHODS

Figure 1 displays the molecular structures of CF, SF, and a monomer unit of D18 studied in this work. CF and SF molecules contain 236 atoms, while D18 comprises 189. To focus on the short-range noncovalent interactions that govern donor–acceptor miscibility and morphological behavior, we modeled the donor polymer D18 using its monomeric unit. While polymer chain conformation and flexibility are important, simulating long polymer chains significantly increases computational cost and introduces complexity related to chain entanglement and self-assembly. Given that dispersion and dipolar interactions operate over short distances, monomer–acceptor models are sufficient to capture the key interaction features relevant to phase morphology.[23−25]

The initial molecular structures of CF, SF, and D18 monomers were constructed using GaussView.[26] These structures were optimized within density functional theory at the B3LYP-D3(BJ)/6−31G(d,p) level. To ensure that the optimized geometries correspond to true local minima, vibrational frequency calculations

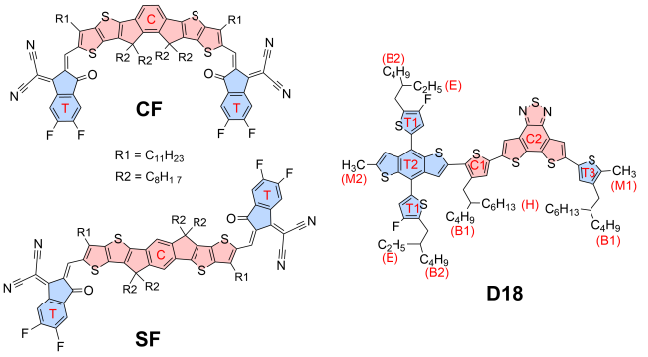

Nomenclature	Description of fragments and side chains
C(1/2)	Core rings
T(1/2/3)	Terminal rings
B(1/2)	End methyl group of the Butyl chain attached to D18
E	End methyl group of the Ethyl chain attached to D18
H	End methyl group of the Hexyl chain attached to D18
M(1/2)	Methyl group attached to D18 terminal rings

Figure 1. Top: Illustration of molecular structures and nomenclature for different fragments in CF, SF, and D18 molecules. Bottom: Definitions used in this study for the fragment labels on NFAs, CF/SF, and D18.

were performed using the Gaussian09 software package.[27] To model bulk amorphous mixtures of pure NFAs and NFA-polymer blends, MD simulations were carried out using the GROMACS engine.[28,29] Accurate force-field parameters for CF, SF, and D18 molecules were generated using the Sobtop program.[30] This approach derives bonded and nonbonded parameters (bonds, angles, and dihedrals) directly from the Hessian matrix obtained via DFT-based frequency calculations. A similar method was utilized in the literature to optimize bonded parameters for organic molecules.[31,32] Atomic charges were assigned based on restrained electrostatic potential (RESP2) calculations performed using the Multiwfn program.[33] Geometry optimizations and DFT-based force field parametrization were carried out using B3LYP/6−31G(d,p), which balances computational efficiency and accuracy well. While this level does not include explicit dispersion, van der Waals interactions were accounted for in MD simulations via Lennard-Jones potentials with a 10 Å cutoff.

To prepare amorphous mixtures, 1000 monomers of CF and SF were randomly packed into a cubic simulation box to generate pure NFA phases. In the blended systems, 500 monomers of D18 were mixed with 600 monomers of either CF or SF. The donor-to-acceptor ratio used in the simulations reflects the experimental weight ratio (1:1.2),[32] which was directly applied to the number of molecules. This simplification ensures consistent comparison between CF:D18 and SF:D18 blends while preserving the experimentally relevant excess of acceptor content. This initial random packing ensured a uniform distribution of molecules, minimizing biases in the starting configuration. All systems underwent an initial energy minimization using the steepest descent algorithm to remove steric clashes. Subsequently, temperature annealing was performed in an NPT ensemble, ramping from 100 to 800 K over 3 ns to enhance molecular mixing and facilitate the attainment of an equilibrated morphology. The simulations employed a canonical velocity rescaling thermostat[34] to maintain temperature control, while pressure was regulated using a Berendsen barostat.[35] Long-range electrostatic interactions were computed using the smooth particle mesh Ewald (PME) method. Following the annealing step, a controlled cooling phase was implemented in two stages: (i) from 800 to 600 K and (ii) from 600 to 300 K, with both steps performed under the same NPT ensemble over an additional 3 ns. This gradual cooling was essential for stabilizing the system morphology and preventing kinetically

https://doi.org/10.1021/acsaem.5c01643
ACS Appl. Energy Mater. XXXX, XXX, XXX−XXX

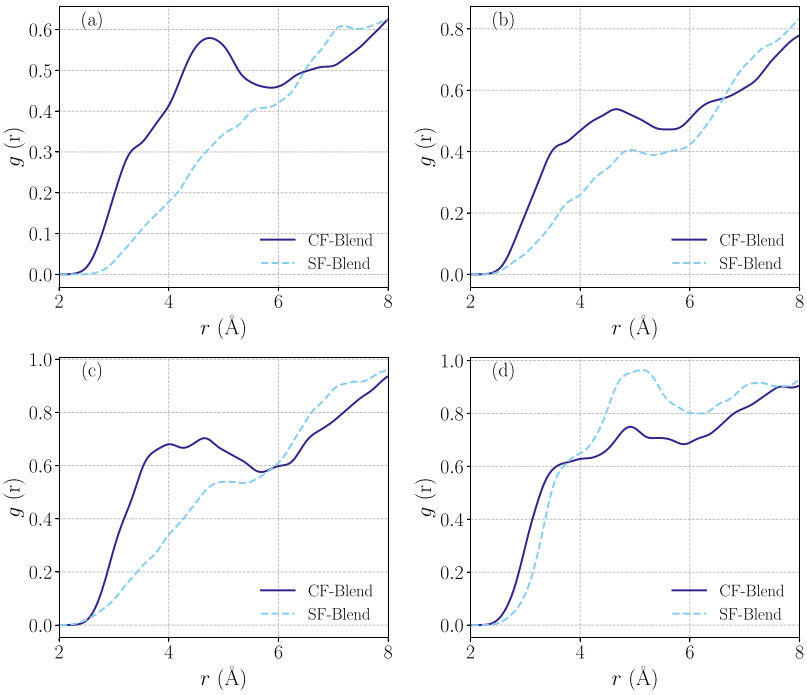

Figure 2. Radial distribution function plots showing the interactions between the π-electron cloud of the central ring (C) in CF/SF molecules and the hydrogen attached to (a) B1, (b) E, (c) M1, and (d) M2 groups of D18 molecules, highlighting differences in C−H···π interactions between CF and SF blend.

trapped configurations. Once cooled to 300 K, the systems were subjected to production MD simulations for an additional 3 ns in the NVT ensemble. The Verlet leapfrog algorithm was used to integrate the equations of motion with a time step of 1 fs.[36] A real-space cutoff of 1.3 nm was applied for nonbonded interactions, and the stability of thermodynamic parameters (temperature, pressure, and potential energy) was verified to ensure equilibrium was reached before analysis. The steps employed in generating amorphous morphologies followed the previous literature reports.[37,38] Structural and interaction analyses were conducted using multiple postprocessing tools. Initial visualization of acceptor−donor interactions was performed using VMD.[39] Radial distribution functions were computed from the MD trajectories using the TRAVIS package[40,41] to quantify key molecular interactions, including CH-π stacking, hydrogen bonding, and halogen interactions.

To investigate the nature of noncovalent interactions (NCI) between donor and acceptor molecules, we employed the NCIPLOT4 package.[42] 100 configurations of D18 monomers located within 6 Å of CF/SF monomers were extracted from the MD trajectory spanning 3 ns. This distance threshold ensured that only molecular pairs exhibiting significant noncovalent interactions were considered. The NCI approach visually and quantitatively represents weak interactions such as CH-π, halogen bonding, and van der Waals forces, which are crucial in blend morphology and charge transport.

Beyond qualitative NCI analysis, we employed *k*-means clustering[43] to classify the molecular packing motifs within the blended systems. *k*-means clustering is an unsupervised machine learning method that partitions data points into distinct clusters based on spatial proximity and structural similarities. In this study, we computed the centroids of conjugated rings representing the backbone chains of D18 and CF/SF molecules. A distance matrix was constructed using these centroid positions to account for interactions between different ring types, including terminal-terminal, core-terminal, and terminal-core contacts. The clustering was performed using the scikit-learn module,[44] to identify dominant packing arrangements and their relative prevalence in each blend.

We performed Voronoi tessellation[45,46] analysis to further characterize the molecular organization and miscibility in the blended systems. This method quantifies the local packing efficiency by partitioning space into Voronoi cells, where each cell represents the spatial domain closest to a given molecule. The molecular volume ratio to local free space provides insight into blend homogeneity and molecular dispersion. Voronoi tessellation was carried out using the OVITO program,[47] with centroid positions of terminal and core rings from D18 and CF/SF molecules serving as input data points. This analysis enabled a comparative evaluation of the free volume distribution in both blends, shedding light on their packing characteristics and phase behavior.

We performed energy decomposition analysis (EDA) using the sobEDA program to better understand donor−acceptor interactions at the electronic structure level.[48] EDA allows the decomposition of the total interaction energy into physically meaningful components, elucidating the key stabilizing forces governing the blend morphology. Specifically, we employed the dispersion-corrected Kohn−Sham DFT (KS-DFT) approach to compute the total interaction energy of donor−acceptor pairs, utilizing the wave functions of the isolated molecular fragments. Given the significance of dispersion interactions in organic electronic materials, we adopted the sobEDAw variant of EDA, which provides a cost-effective alternative to symmetry-adapted perturbation theory (SAPT).[49,50] The sobEDAw method introduces a weighting function (w) to partition the DFT correlation energy (ΔE_{DFTc}) into two terms: one incorporated into the dispersion correction (ΔE_{disp}) and the other combined with exchange-repulsion (ΔE_{xrep}). This approach effectively captures midrange Coulomb correlation while ensuring a balanced treatment of dispersion interactions. We adopted the computational protocol recommended by Lu and Chen,[48] using the B3LYP-D3(BJ) functional with the 6−31+G(d,p) basis set. We employed the same level of theory, which incorporates empirical dispersion corrections, to perform energy decomposition analysis aimed at accurately capturing noncovalent interactions. Prior benchmarking studies (e.g., Balci et al.[51]) support the reliability of this approach for systems involving weak intermolecular forces. Five random donor−acceptor dimer pairs were extracted for EDA calculations for each blend. The decomposed energy components included electrostatics (ΔE_{els}), exchange-repulsion (ΔE_{xrep}), orbital interactions (ΔE_{orb}), and dispersion correction (ΔE_{disp}), which correspond well to SAPT terms (ΔE_{els}, ΔE_{exch}, ΔE_{ind}, and ΔE_{disp}, respectively). The cost-effectiveness and

https://doi.org/10.1021/acsaem.5c01643
ACS Appl. Energy Mater. XXXX, XXX, XXX−XXX

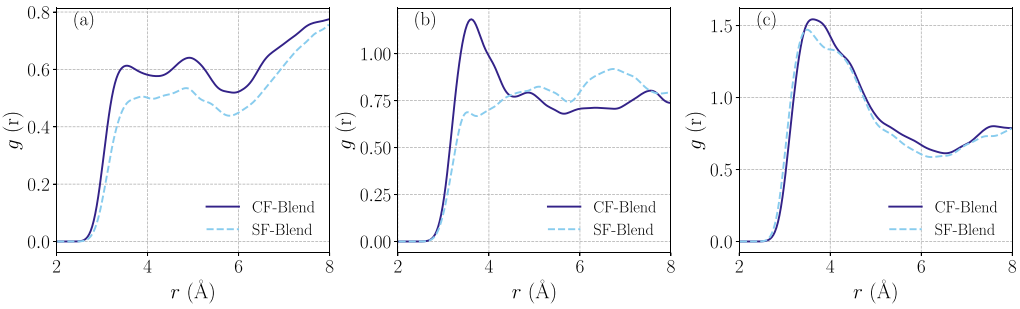

Figure 3. (a) RDF plot between the fluorine atom of D18 molecules and the sulfur atom in CF/SF molecules. (b, c) RDF plots between the oxygen atom of CF/SF molecules and the sulfur atom attached to the (b) terminal ring (T3) and (c) core ring (C2) of D18 molecules, respectively.

accuracy of the sobEDAw method make it a reliable alternative for analyzing weak donor−acceptor interactions in large molecular systems.

3. RESULTS AND DISCUSSION

Recent studies have highlighted the impact of molecular geometry on the performance of NFAs in organic solar cells, showing that C-shaped NFAs facilitate the formation of a well-defined fibrillar network when blended with the D18 polymer, in contrast to S-shaped NFAs.[22] Given the crucial role of weak interactions in determining blend morphology, as established in our previous work,[23] we first screened potential donor−acceptor interactions based on distance criteria and performed RDF analysis to assess the clustering of D18 molecules around CF and SF monomers. This preliminary analysis provided insight into the nature of noncovalent interactions, such as hydrogen bonding and van der Waals forces, that drive molecular aggregation and influence phase behavior in these blends. To ensure clarity in describing specific molecular fragments, side chains, and functional groups within NFAs and the polymer matrix, we have adopted a custom nomenclature, as detailed at the bottom of Figure 1. This nomenclature is consistently used throughout the manuscript to maintain precision in our discussion of molecular interactions.

Among the various noncovalent interactions, van der Waals forces are particularly significant in systems containing aromatic components. The $\pi-\pi$ stacking interaction between π-electron cloud of aromatic rings is known to play a critical role in determining packing motifs in organic semiconductors. To evaluate its contribution to the CF/SF−D18 blends, we computed radial distribution functions between the centers of the geometry of the aromatic rings in CF/SF and D18 molecules. The corresponding RDFs, shown in Figure S1, do not exhibit any pronounced peaks within the characteristic $\pi-\pi$ stacking distance range (3.3−5.8 Å), indicating negligible face-to-face interactions between the π-systems. This suppression of stacking can be attributed to the bulky aliphatic side chains present on both CF/SF and D18, which sterically hinder efficient $\pi-\pi$ overlap. Notably, this observation is consistent with our earlier work on similar conjugated polymer blends relevant to organic solar cells, where $\pi-\pi$ interactions were also found to be weak or absent.[23]

Additionally, van der Waals interactions often manifest as C−H···π interactions, where a C−H group donates to an aromatic ring's π-electron cloud. These interactions arise primarily from a combination of dispersion and electrostatic forces, with negligible contributions from hydrophobic effects. Our previous studies on NFA−polymer blends have demonstrated that such van der Waals interactions play a key role in stabilizing blend morphology,[23] underscoring their importance in the self-assembly and miscibility of donor−acceptor pairs in OSCs.

Building on our discussion of van der Waals interactions, Figure 2 reveals that CF blend exhibit stronger C−H···π interactions between the π-electron clouds of core rings (NFA) and hydrogen atoms from various methyl-containing groups in D18 (B1, E, M1, and M2) compared to SF blend. Notably, the B1 group in CF blend displays a distinct RDF peak at approximately 4.7 Å, whereas no corresponding peak is observed in SF blend (Figure 2a), suggesting a more favorable packing arrangement in CF-based systems. Similarly, the M1 group in CF blend exhibits a broad peak around 4.3 Å, absent in SF blend (Figure 2c), further highlighting the enhanced van der Waals interactions in CF-based blend. Steric effects arising from the bulky molecular structures influence the packing efficiency, leading to broader RDF peaks for methyl groups on the terminal rings of D18 interacting with the core π clouds of CF and SF molecules. This effect is particularly evident for the E group, where the RDF peak in CF blend is significantly broadened and exhibits increased intensity around 4.5 Å compared to SF blend (Figure 2b), indicating stronger C−H···π interactions in CF blend. Additionally, while SF blend show a pronounced RDF peak for M2 at approximately 5 Å, CF blend exhibit a peak slightly below 5 Å with a noticeable shoulder near 3 Å (Figure 2d), suggesting that CH···π interactions are more prevalent in CF-based systems. These findings reinforce the idea that the molecular geometry of CF facilitates stronger van der Waals interactions, potentially contributing to its enhanced miscibility in blend with D18.

Hydrogen bonding arises when a hydrogen atom, covalently bonded to an electronegative donor (D), interacts with an electronegative acceptor (A), typically involving elements such as oxygen, nitrogen, sulfur, and fluorine. A visual illustration of random snapshots showing hydrogens involved in C−H···F interactions in blended systems is presented in Figure S2. During the analysis, a commonly accepted threshold (bond distance $\lesssim$3.0 Å) was used to identify weak hydrogen bonds, including those involving nontraditional donors such as C−H. As shown in Figure S3a, CF blend exhibit a distinct RDF peak at approximately 2.8 Å, corresponding to hydrogen bonds between the M1 group of D18 and oxygen atoms. This peak is notably absent in SF blend. Conversely, Figure S3c shows a pronounced RDF peak at a similar distance for hydrogen bonds between the M2 group of D18 and oxygen atoms in SF blend. A similar interaction is also seen in the CF:D18 blend with a lower peak height. Hydrogen bonds involving fluorine or nitrogen are generally weaker than those with oxygen. Figure S3b reveals a moderately enhanced RDF peak in SF

https://doi.org/10.1021/acsaem.5c01643
ACS Appl. Energy Mater. XXXX, XXX, XXX−XXX

blend at around 2.9 Å, corresponding to hydrogen bonding between the hydrogen atoms of the M1 group in D18 and the fluorine atoms in CF/SF molecules. Meanwhile, Figure S3d shows that CF blend exhibit a slightly stronger hydrogen bonding peak at approximately 3.0 Å between the M2 group of D18 and nitrogen atoms in NFA. Additionally, weak hydrogen bonds involving the methyl hydrogens of D18 and the nitrogen or fluorine atoms in CF/SF molecules are observed at around 3.0 Å, with alternating enhancements between CF and SF blend, as shown in Figure S4. These observations suggest these weak hydrogen bonds contribute comparably in both systems, reinforcing the overall noncovalent interaction landscape.

Noncovalent interactions involving sulfur (S) with oxygen (O) or fluorine (F) atoms also contribute significantly to weak interactions in these blends. As shown in Figure 3a, the RDF analysis reveals a broad peak around 3.5 Å for the interaction between the fluorine atom of D18 and the sulfur atom of CF, with a higher probability than in SF blend. Similarly, the sulfur atom on the terminal ring (T3) of D18 exhibits a distinct RDF peak at approximately 3.6 Å with oxygen atoms in CF blend, whereas this interaction is absent in SF blend (Figure 3b). In contrast, the interaction between the sulfur atom on the core ring (C2) of D18 and oxygen atoms occurs at 3.6 Å in SF blend and shifts to 3.8 Å in CF blend, with comparable probabilities (Figure 3c). These results suggest that noncovalent interactions are more pronounced in the CF blend than in the SF blend, further influencing their molecular packing and overall stability.

3.1. NCI Analysis. Noncovalent interactions in molecular systems can be effectively analyzed by examining the electron density, $\rho(r)$, and its spatial variations. Using NCIPLOT, weak interactions are identified by locating electron density critical points ($\nabla\rho = 0$) that arise during atomic interactions.[42] These regions are indexed based on ρ and its derivatives, allowing a detailed characterization of noncovalent interactions. The reduced density gradient (RDG), a key parameter in this analysis, is plotted against the electron density, providing a two-dimensional representation of weak interactions. RDG is defined using the following equation.[52]

$$\mathrm{RDG}(r) = \frac{1}{2(3\pi^2)^{1/3}} \frac{|\nabla\rho(r)|}{\rho^{4/3}} \quad (1)$$

In low-density regions far from the molecule, where ρ decays exponentially, RDG exhibits large positive values. However, near critical points, where the gradient of ρ dominates, RDG approaches zero, forming characteristic troughs that signal weak interactions. This method relies on promolecular electron density estimates, avoiding artifacts from electronic relaxation typically introduced in self-consistent field calculations such as Hartree−Fock or density functional theory.

Further analysis of electron density troughs is necessary to determine the nature of these weak interactions—whether they arise from steric effects, hydrogen bonding, or van der Waals forces. While the electron density in these regions provides insight into interaction strength, both attractive (e.g., hydrogen bonds) and repulsive (e.g., steric effects) interactions may coexist in the same RDG space.

The Laplacian of the electron density ($\nabla^2\rho$), representing the net flux of electron density in a given region, can help distinguish between attractive and repulsive interactions. A negative $\nabla^2\rho$ indicates electron density accumulation, characteristic of bonding interactions, while a positive $\nabla^2\rho$ signifies density depletion, often associated with steric repulsion. However, since $\nabla^2\rho$ is dominated by the strong negative contributions near nuclei, it does not provide a direct classification of weak interactions. Instead, decomposition into three principal eigenvalues (λ_1, λ_2, λ_3) offers a more refined approach, with $\lambda_1 < \lambda_2 < \lambda_3$ such that $\nabla^2\rho = \lambda_1 + \lambda_2 + \lambda_3$. Near nuclear positions, all eigenvalues are negative, whereas away from nuclei, λ_3 becomes positive.

For noncovalent interactions, the sign of the second eigenvalue (λ_2) is particularly useful. A negative λ_2 ($\lambda_2 < 0$) indicates density accumulation perpendicular to the bond, typical of attractive interactions such as hydrogen bonding. Conversely, steric repulsion depletes density, leading to a positive λ_2, while van der Waals interactions, characterized by minimal density overlap, yield λ_2 values close to zero ($\lambda_2 \approx 0$). Therefore, the sign of λ_2 effectively differentiates weak interactions, while the electron density magnitude reflects their strength.[53]

The RDG plot (Figure S5) visually represents these interactions, where attractive forces appear in green and blue—indicating van der Waals interactions [$(\mathrm{sign}\lambda_2)\rho \approx 0$] and hydrogen bonds [$(\mathrm{sign}\lambda_2)\rho < 0$], respectively—while repulsive steric interactions are shown in red due to positive $(\mathrm{sign}\lambda_2)\rho$ values.[54] The RDG analysis further reveals that CF blend exhibit stronger van der Waals interactions than SF blend, as indicated by the more prominent regions in the $(\mathrm{sign}\lambda_2)\rho$ distribution around the value of zero.

To quantify the strength of these interactions, the integral density was computed over a range of $(\mathrm{sign}\lambda_2)\rho$ values from −0.1 to 0.1, dividing interactions into three categories: strongly attractive (−0.1 a.u. $\leq (\mathrm{sign}\lambda_2)\rho <$ −0.02 a.u.), weak van der Waals interactions (−0.02 a.u. $\leq (\mathrm{sign}\lambda_2)\rho \leq$ 0.02 a.u.), and repulsive interactions (0.02 a.u. $< (\mathrm{sign}\lambda_2)\rho \leq$ 0.1 a.u.). The variation in integral density over MD trajectories for the attractive, van der Waals, repulsive, and total interaction regions is shown in Figure S6. Previous studies have shown that lower integral density values correlate with stronger binding energies.[55]

As summarized in Table 1, the total mean electron density in the CF blend (0.0165) is slightly lower than in the SF blend (0.0194), indicating stronger noncovalent interactions in the CF system. The mean integral density in the attractive region is marginally lower for the CF blend (0.0040) than the SF blend (0.0049), while in the van der Waals region, the CF blend also exhibits a lower integral density (0.0112) compared to the SF blend (0.0132). This trend suggests that the CF blend experiences enhanced attractive and van der Waals interactions. Meanwhile, steric repulsion, which counteracts these attractive forces, remains nearly identical between the two systems. Overall, the predominance of noncovalent interactions over steric effects results in tightly bound systems in both cases, with the CF blend exhibiting slightly stronger binding than the SF blend.

Table 1. Mean Value of Integral Density in Different Regions Corresponding to NCI Analysis

system	ρ_{tot}	ρ_{elec}	ρ_{Vdw}	ρ_{repul}
CF:D18	0.0165	0.0040	0.0112	0.0012
SF:D18	0.0194	0.0049	0.0132	0.0013

3.2. Energy Decomposition Analysis. We further performed a DFT-based energy decomposition analysis to

https://doi.org/10.1021/acsaem.5c01643
ACS Appl. Energy Mater. XXXX, XXX, XXX−XXX

elucidate the nature of noncovalent interactions in these systems. This method breaks down the total interaction energy into its fundamental components, providing deeper insight into the dominant forces that govern binding stability. The key contributors—electrostatic interactions, orbital (induction) effects, and dispersion forces—were analyzed to determine their relative significance in the CF and SF blends. As summarized in Table 2, electrostatic interactions, which are particularly influential at larger intermolecular distances, are noticeably stronger in the CF:D18 blend (−9.0 kcal/mol) than in the SF:D18 blend (−6.9 kcal/mol). This 30.4% increase in electrostatic stabilization enhances intermolecular binding in the CF system. Likewise, orbital (or induction) interaction energy, which accounts for polarization effects arising from the permanent multipoles of one monomer polarizing the electron density of the other, is primarily attributed to dipole−dipole contributions and is used here to describe dipole−dipole interactions. It contributes more significantly to the CF:D18 blend (−4.3 kcal/mol) than the SF:D18 blend (−3.6 kcal/mol), indicating stronger dipole interactions and increased electronic stabilization in CF.

Table 2. Decomposed Energy Components (in kcal/mol) from DFT-Based Energy Decomposition Analysis (EDA) for CF:D18 and SF:D18 Blends[a]

system	electrostatic	exchange-repulsion	orbital	dispersion
CF:D18	−9.0 (30.4%)	29.6 (18.4%)	−4.3	−39.9 (21.3%)
SF:D18	−6.9	25.0	−3.6	−32.9

[a]The percentage values represent the relative difference between the CF and SF blends for each energy component.

Dispersion interactions emerge as the dominant attractive force in both systems, aligning with the enhanced van der Waals interactions previously identified in the RDF and NCI analyses. The CF:D18 blend exhibits a significantly stronger dispersion contribution (−39.9 kcal/mol) than the SF:D18 blend (−32.9 kcal/mol), reinforcing the conclusion that van der Waals forces play a crucial role in stabilizing the CF system. Although exchange-repulsion is higher in the CF:D18 blend (29.6 kcal/mol) than in the SF:D18 blend (25.0 kcal/mol), the net interaction remains stronger in CF:D18 due to the greater attractive contributions from dispersion and induction. Overall, the EDA results are in excellent agreement with the RDG-based NCI analysis, confirming that noncovalent interactions, particularly dispersion and electrostatics, play a pivotal role in dictating the stability of these blends. The enhanced attractive interactions in the CF system lead to a more tightly bound and stable molecular arrangement compared to the SF blend.

3.3. *k*-Means Clustering Analysis. To quantitatively assess the molecular packing in CF and SF blends, we applied machine learning-based clustering analysis using distance matrices derived from MD trajectories. The centroids of key molecular fragments—terminal-terminal (TT), terminal-core (TC), and core−core (CC) rings—were extracted for each NFA-polymer dimer to construct the distance matrices. Figure 4c shows a schematic representation of this process, while Figure 4a,b illustrates the distribution of these centroids in CF and SF blends. The final distance matrix for CF blend comprises 2228 data points, whereas, for SF blend, it contains 2108 data points. To ensure robust clustering and avoid overfitting to noise in these data points, we determined the optimal number of clusters using both the elbow method and the Calinski-Harabasz Index. These approaches evaluate the trade-off between model complexity and within-cluster compactness, allowing us to identify the number of clusters that best capture the intrinsic structure of the data without introducing artificial segmentation.

3.3.1. Optimal Clustering via k-Means. To identify distinct packing motifs within the blends, we employed *k*-means clustering, a widely used unsupervised learning algorithm that partitions data into *k* clusters by minimizing the within-cluster sum of squares (WCSS).[56] However, determining the optimal number of clusters (*k*) is nontrivial. We first applied the elbow method, which involves computing WCSS for a range of *k* values (typically 1 to 20) and identifying the inflection point in the WCSS curve, often termed the "elbow". This point suggests a balance between cluster compactness and computational efficiency.

To further validate the optimal *k* value obtained from the elbow method, we employed the Calinski-Harabasz Index (CHI).[57] While the elbow method relies on subjective interpretation of distortion trends, the CHI offers a robust, quantitative alternative by evaluating the ratio of between-cluster variance to within-cluster variance. CHI evaluates the quality of clustering results by balancing two fundamental characteristics: cluster separation and cluster compactness.

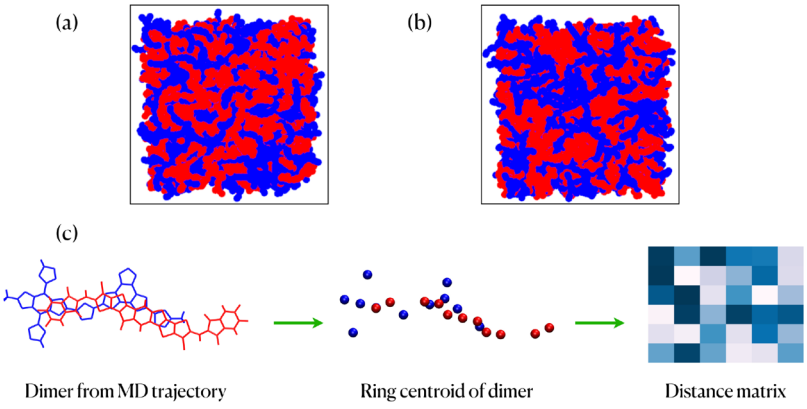

Figure 4. Analysis of molecular packing in CF and SF blends using centroid-based distance matrices. Visualization of the centroid positions of NFA-polymer rings in (a) CF and (b) SF blend. (c) Schematic representation of the workflow for constructing a distance matrix based on terminal-terminal (TT), terminal-core (TC), and core−core (CC) ring distances in the MD trajectory.

https://doi.org/10.1021/acsaem.5c01643
ACS Appl. Energy Mater. XXXX, XXX, XXX−XXX

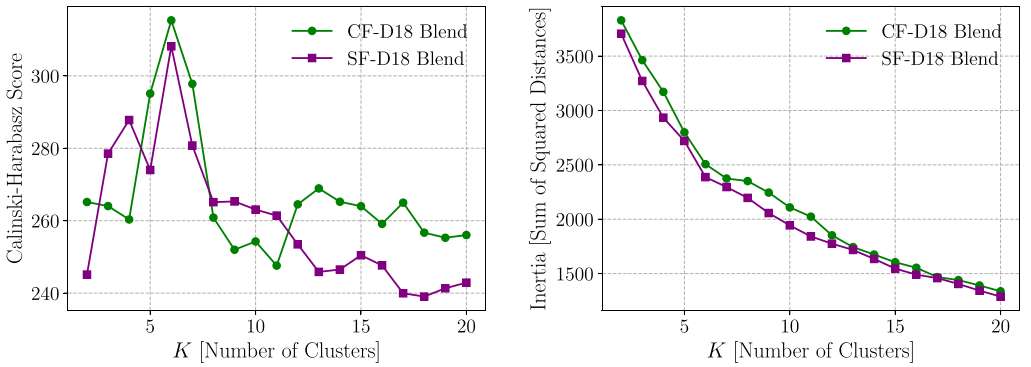

Figure 5. Determination of the optimal number of clusters (k) for k-means clustering in CF and SF blends. (left) Calinski-Harabasz Index (CHI) scores as a function of cluster numbers, indicating the optimal k. (right) Inertia plot (Elbow method) showing the within-cluster sum of squares (WCSS) for different k values.

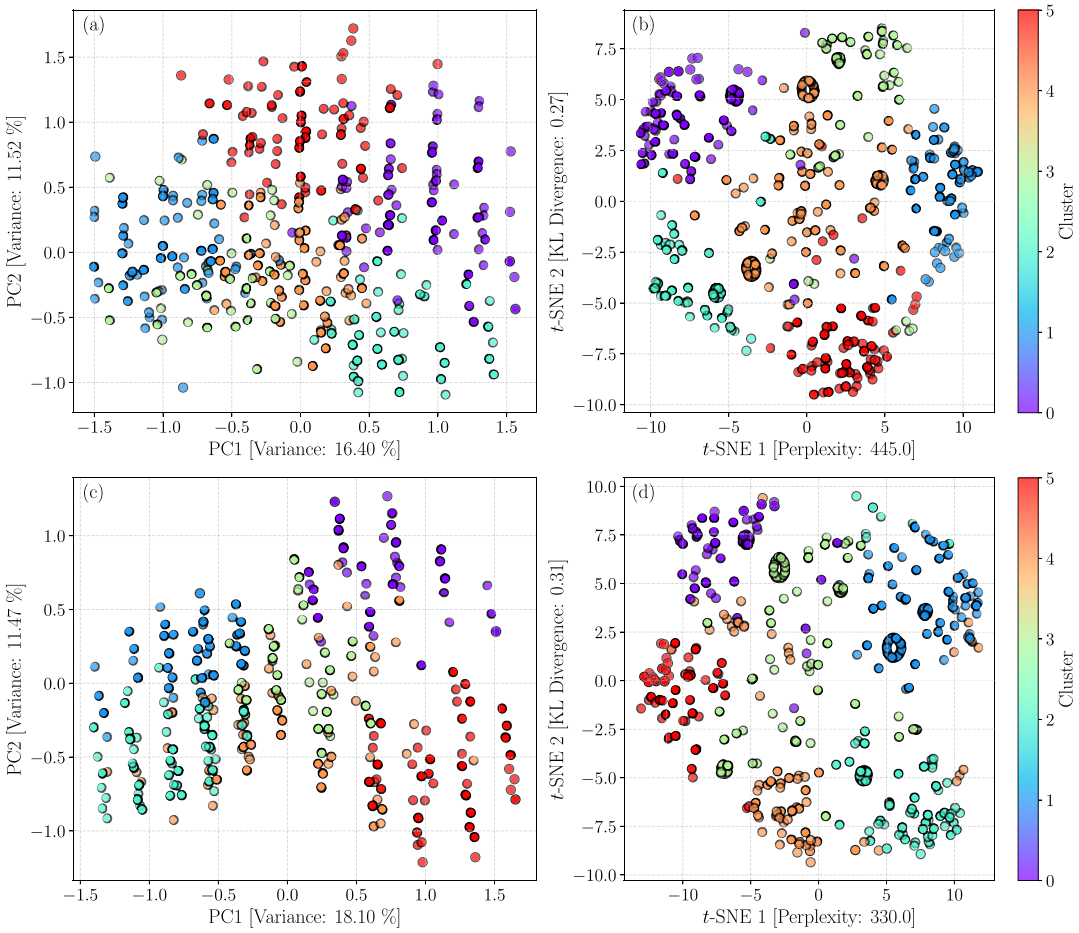

Figure 6. Two-dimensional visualization of k-means clustering (k = 6) for CF and SF blends: (a, c) Principal Component Analysis (PCA) plots for CF and SF blends show the distribution of clusters in the first two principal components. (b, d) t-distributed Stochastic Neighbor Embedding (t-SNE) plots for CF and SF blends, revealing distinct clustering patterns based on nonlinear relationships.

Cluster separation refers to how distinctly different clusters are from one another, measured by the spread of their central points relative to the overall data set's center. Cluster compactness assesses how closely grouped data points are within their assigned clusters, calculated by the average proximity of points to their cluster's central reference. The CHI score is defined as

$$\mathrm{CHI} = \frac{\text{Between-Cluster Variance}\left(\sum_{i=1}^{k} n_i \left\| c_i - c \right\|^2\right)/(k-1)}{\text{Within-Cluster Variance}\left(\sum_{i=1}^{k}\sum_{x\in C_i} \left\| x - c_i \right\|^2\right)/(n-k)} \quad (2)$$

where k is the number of clusters, n_i is the number of data points in cluster i, c_i is the centroid of cluster i, c is the global centroid of the data set, and C_i is the set of points in cluster i. A

https://doi.org/10.1021/acsaem.5c01643
ACS Appl. Energy Mater. XXXX, XXX, XXX−XXX

higher CHI score indicates clusters that are both well-separated and compact. To determine the optimal k value, k-means clustering was iteratively applied over a range of k values, and the value of k that yields the maximum CHI score was selected. This method automates cluster selection by eliminating the visual subjectivity inherent in the elbow method while also ensuring computational efficiency and scalability. As shown in Figure 5, both the elbow method and CHI analysis consistently suggest six as the optimal number of clusters for both CF and SF blends. However, due to the differences in data set sizes between the two blends, direct comparison of CHI or elbow scores does not provide an absolute measure of clustering quality.

3.3.2. Cluster Visualization and Structural Interpretation. After determining the optimal number of clusters, we applied two dimensionality reduction techniques to visualize the clustering results: Principal Component Analysis (PCA) and t-distributed Stochastic Neighbor Embedding (t-SNE).

3.3.2.1. PCA-Based Cluster Analysis. PCA was selected because it can efficiently reduce the data set's dimensionality while preserving as much variance as possible. It is defined as an orthogonal linear transformation that projects the data onto a lower-dimensional subspace, known as the principal subspace, such that the first coordinate (the first principal component) captures the greatest variance, the second coordinate the next highest variance, and so on. PCA offers a linear transformation that can be readily interpreted in terms of the original variables, and the transformation is expressed as

$$Y = WX \tag{3}$$

where Y represents the transformed data (principal components), W is the eigenvectors of the covariance matrix (principal component coefficients), and X represents the mean-center data matrix with dimensions $n \times p$ (n, samples, p, features).

As shown in Figure 6a,c, PCA analysis indicates that the first principal component (PC1) accounts for 16.40% of the variance in CF blend and 18.10% in SF blend, suggesting that CF blend exhibit more distributed molecular interactions. In contrast, the second principal component (PC2) contributes nearly equally in both cases (CF: 11.52%, SF: 11.47%). The two-dimensional PCA plot reveals that clusters in CF blend are less well-separated than those in SF blend, indicating a more homogeneous distribution of molecular fragments in CF blend (less segregation) compared to SF blend, where distinct molecular packing motifs emerge (more segregated morphology).

3.3.2.2. t-SNE-Based Cluster Analysis. To complement PCA, we applied t-SNE, a nonlinear dimensionality reduction method that preserves local relationships and helps visualize clustering patterns. t-SNE converts high-dimensional Euclidean distances into conditional probabilities representing similarities between data points. This approach is beneficial because it reveals complex patterns that might not be apparent using linear techniques like PCA.

t-SNE primarily aims to minimize the Kullback–Leibler (KL) divergence between a high-dimensional probability distribution P and a corresponding low-dimensional distribution Q. The KL divergence quantifies the dissimilarity between these two distributions. Subsequently, t-SNE employs an iterative algorithm that adjusts the positions of points in the low-dimensional space so that Q closely approximates P. This is accomplished by minimizing a cost function, C, through a gradient descent method that determines the direction and magnitude of the necessary adjustments. The cost function C is defined as follows:

$$C = KL(P||Q) = \sum_i \sum_j p_{j|i} \ln\left(\frac{p_{j|i}}{q_{j|i}}\right) \tag{4}$$

where P and Q represent high- and low-dimensional distributions, respectively.

As shown in Figure 6b,d, t-SNE visualizations confirm the clustering trends observed in PCA. The CF blend exhibits a broad dispersion of points along the t-SNE1 and t-SNE2 axes, indicating a more continuous distribution of molecular fragments and weaker clustering patterns. Although local groupings exist, the boundaries between clusters in the CF blend are not sharply defined. In contrast, the SF blend forms well-separated, compact clusters, signifying a more distinct molecular packing arrangement. Overall, SF blend demonstrates superior clustering quality, with k-means identifying six well-separated clusters that achieve a better balance between intracluster cohesion and intercluster separation. Notably, the perplexity parameter, which determines the balance between local and global structure, was optimized using the silhouette score. The CF blend was best represented with a perplexity of 445.0 (KL divergence: 0.27), whereas the SF blend required a lower perplexity of 330.0 (KL divergence: 0.31), suggesting that SF blend exhibit a more localized packing structure.

The clustering analysis provides critical insights into the morphological differences between CF and SF blends:

- CF blend exhibit more uniform packing, with molecular fragments more evenly distributed across the system, leading to a more continuous and less segregated morphology. This dense mixing suggests strong intermolecular interactions, potentially contributing to better charge transport properties.
- On the other hand, SF blend demonstrate well-defined clusters, indicating a segregated molecular packing arrangement where TT, TC, and CC rings remain more distinctly grouped. This suggests a preference for phase-separated domains, which could influence mechanical properties and charge transport pathways differently than CF blend.

The machine learning-based clustering approach reveals that CF blend promote a more homogeneous mixing of molecular fragments, whereas SF blend tend to form distinct molecular aggregates. These findings align with our previous analyses, including RDF and NCI results, highlighting stronger dispersion interactions and reduced phase segregation in CF blend.

3.4. Voronoi Analysis. Voronoi analysis, a geometric partitioning technique, divides space into regions (cells) surrounding discrete points, such as phase domains or molecular centroids, where each point within a given cell is closer to its central site than any other. Constructed using perpendicular bisectors between neighboring sites, Voronoi tessellations provide a robust framework for analyzing spatial distributions in polymer blends.[58,59] When applied to phase-separated systems, this method enables quantification of microstructural uniformity, pore distribution, and domain arrangement by statistically evaluating cell areas and coordination numbers. For instance, Voronoi diagrams of EVA/PMMA copolymer blends revealed that reduced pore

https://doi.org/10.1021/acsaem.5c01643
ACS Appl. Energy Mater. XXXX, XXX, XXX−XXX

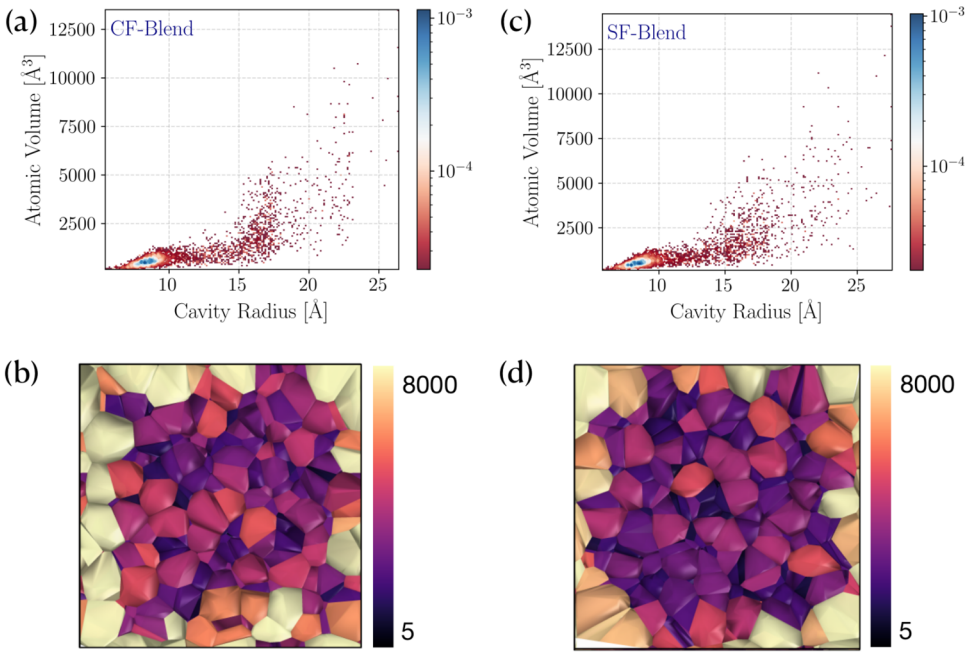

Figure 7. Probability distribution of atomic volume as a function of cavity radius for (a) CF and (b) SF blends, illustrating differences in molecular packing and void distribution. Voronoi tessellations of (c) CF and (d) SF blends, where the color gradient represents Voronoi cell volumes, highlighting variations in spatial organization and packing efficiency.

diameters and enhanced uniformity improved mechanical properties.[60] Similarly, breath-figure patterns on polystyrene surfaces were analyzed using Voronoi polygons to assess droplet coordination and 6-fold symmetry, linking morphology to solvent volatility and humidity.[61] A key advantage of the Voronoi-based approach is its computational efficiency, which eliminates the need for resource-intensive simulations. This technique bridges statistical morphology with predictive modeling by transforming complex microstructures into quantifiable geometric parameters, making it a versatile tool for optimizing polymer blend design.

In our study, Voronoi analysis was performed using the centroids corresponding to nonfullerene acceptors' terminal and core regions and polymers extracted from molecular dynamics trajectories, similar to the clustering approach used in *k*-means analysis. We analyzed the probability distribution of atomic volume versus cavity radius to evaluate the miscibility and packing efficiency of polymer blends. Here, the cavity radius represents the largest empty space adjacent to a given particle, while atomic volume quantifies the local territory occupied by the particle through its Voronoi cell. A strong positive correlation between Voronoi volume and cavity radius suggests loose packing with defect-rich regions, whereas a weak or negative correlation indicates dense molecular environments or aspherical cavities. Thus, data points with smaller cavity radii relative to Voronoi volumes signify efficient packing, while larger cavities highlight structural imperfections or functional voids.

Figure 7a shows the distribution of atomic volume and cavity radius for CF blend. The data points exhibit tight clustering up to cavity radii of approximately 17.5 Å and atomic volumes around 5000 Å^3, indicative of efficient molecular packing with minimal void spaces. This suggests a homogeneous microstructure dominated by cohesive interactions. Although our simulations are limited in capturing mesoscale fibrillar structures, the observed enhanced donor−acceptor miscibility and local morphological homogeneity in the CF:D18 system suggest contributing to enhanced mechanical stability. This inference aligns with previous experimental findings, where increased miscibility in polymer blends such as EVA/PMMA[60] and PVDF/PLLA[62] was shown to enhance tensile strength, fracture toughness, and elongation at the breaking through more uniform morphology and better stress transfer between phases. In contrast, SF blend (Figure 7b) display a broader distribution extending to larger cavity radii (19.5 Å) and atomic volumes (~6000 Å^3), reflecting localized segregation and loose packing. The positive correlation between these parameters in SF blend supports the presence of aspherical cavities or structural imperfections, likely stemming from incompatibilities in NFA-polymer interactions. Overall, the reduced cavity radii and atomic volumes in CF blend indicate superior mechanical stability, whereas the broader distribution in SF blend highlights regions susceptible to stress concentration. These findings align with previous studies linking Voronoi metrics to material performance,[60] further validating the use of geometric partitioning techniques for assessing polymer blend morphology.

Figure 7c,d depict Voronoi tessellations of particles, with a color gradient representing the volumes of the Voronoi cells. Based on the visual representation of the Voronoi cell distributions, distinct differences emerge between the CF and SF blends. The CF blend exhibits a more uniform distribution of cell sizes, especially in the central region, where a predominance of purple and magenta cells arranged compactly suggests efficient molecular packing. Conversely, the SF blend displays greater variability in cell sizes and shapes, with a less organized distribution of color components. This heterogeneity and more pronounced gaps and irregularities between adjacent cells visually confirm the presence of aspherical cavities and a looser packing arrangement compared to the CF blend.

https://doi.org/10.1021/acsaem.5c01643
ACS Appl. Energy Mater. XXXX, XXX, XXX−XXX

These visual distinctions correlate strongly with the quantitative findings from the probability distribution analysis. The compact and uniform structure of the CF blend's Voronoi cells aligns with the observed tight clustering in the atomic volume versus cavity radius plot, further substantiating the homogeneous microstructure and minimal void spaces. In contrast, the SF blend's more varied cell sizes and irregular shapes reflect the broader distribution in its atomic volume and cavity radius data, supporting the interpretation of localized segregation and looser packing. The visual evidence reinforces the conclusion that the CF blend exhibits superior morphological homogeneity compared to the SF blend.

4. CONCLUSIONS

Our study highlights the critical role of noncovalent interactions in determining the stability and structural integrity of CF and SF polymer blends. Radial distribution function and noncovalent interaction analyses reveal that despite their similar isomeric structures and comparable electronic properties, subtle differences in geometrical configurations lead to stronger van der Waals and dipole−dipole interactions in the CF blend. Energy decomposition analysis further supports these findings, showing that electrostatic and dispersion interactions contribute more significantly to the stability of the CF blend, reinforcing their superior NFA-polymer binding.

The absence of characteristic $\pi-\pi$ stacking in within the characteristic $\pi-\pi$ stacking range (3.3−5.8 Å) in either blend is consistent with prior findings in polymer−fullerene and polymer-NFA systems where bulky side chains sterically hinder ordered stacking.[63,64] Instead, local packing in both CF:D18 and SF:D18 blends is governed by alternative noncovalent interactions such as C−H···π and C−H···O contacts involving side chains and aromatic moieties. NCI analysis and energy decomposition revealed that these interactions are stronger and more frequent in the CF blend compared to the SF blend. These results indicate that the CF blend exhibits more favorable packing not through conventional $\pi-\pi$ stacking but via enhanced cohesive noncovalent interactions and denser local organization.

k-means clustering analysis demonstrates that machine learning techniques provide valuable insights into the miscibility of NFA−polymer systems. The results indicate that CF blend exhibit a well-mixed distribution of terminal-terminal, terminal-core, and core−core interactions, while SF blend show more segregated and clustered arrangements. This poor miscibility in SF blend is likely a key factor in their reduced power conversion efficiency, aligning with previous experimental observations.

Voronoi analysis further substantiates these findings by offering a geometric perspective on molecular packing. The CF blend displays a more uniform distribution of Voronoi cell sizes, indicative of efficient molecular packing with minimal void spaces. In contrast, the SF blend exhibits greater cell size and shape variability, with larger cavities and structural irregularities that suggest localized segregation. The combination of quantitative (probability distribution functions) and visual (Voronoi tessellation) analyses confirms that CF blend form a more cohesive and mechanically stable morphology, whereas SF blend are prone to defects and looser packing.

Overall, our results emphasize that even slight variations in the isomeric configuration of NFAs can profoundly affect noncovalent interactions within a polymer matrix. These differences directly influence the blends' miscibility, stability, and mechanical performance, ultimately impacting their suitability for organic electronic applications. By integrating molecular simulations with data-driven techniques such as *k*-means clustering and Voronoi analysis, this study provides a comprehensive framework for understanding and optimizing NFA−polymer interactions in next-generation materials.

■ ASSOCIATED CONTENT

Data Availability Statement

The molecular structures, force field parameters, and topology files utilized in this study are in a separate compressed file (data.zip) and can be applied to reproduce the outcomes reported.

Supporting Information

The Supporting Information is available free of charge at https://pubs.acs.org/doi/10.1021/acsaem.5c01643.

The Supporting Information contains radial distribution functions, reduced density gradients, and NCI density (PDF)

Data (ZIP)

Input coordinates (ZIP)

■ AUTHOR INFORMATION

Corresponding Author

Anirban Mondal − *Department of Chemistry, Indian Institute of Technology Gandhinagar, Gandhinagar, Gujarat 382355, India;* orcid.org/0000-0003-3029-8840; Email: amondal@iitgn.ac.in

Authors

Ram Sewak − *Department of Chemistry, Indian Institute of Technology Gandhinagar, Gandhinagar, Gujarat 382355, India;* orcid.org/0000-0001-5700-0122

Krishna Singh − *Department of Chemistry, Indian Institute of Technology Gandhinagar, Gandhinagar, Gujarat 382355, India*

Complete contact information is available at: https://pubs.acs.org/10.1021/acsaem.5c01643

Author Contributions

A.M. conceived the problem. R.S. and K.S. conducted all the simulations. R.S., K.S., and A.M. analyzed the results. R.S. and A.M. prepared the draft.

Notes

The authors declare no competing financial interest.

■ ACKNOWLEDGMENTS

The authors gratefully acknowledge the Indian Institute of Technology Gandhinagar, India, for providing research facilities and financial support. The authors thank PARAM Ananta for computational resources.

■ REFERENCES

(1) Hou, J.; Inganäs, O.; Friend, R. H.; Gao, F. Organic solar cells based on non-fullerene acceptors. *Nat. Mater.* **2018**, *17*, 119−128.

(2) Liu, S.; Yuan, J.; Deng, W.; Luo, M.; Xie, Y.; Liang, Q.; Zou, Y.; He, Z.; Wu, H.; Cao, Y. High-efficiency organic solar cells with low non-radiative recombination loss and low energetic disorder. *Nat. Photonics* **2020**, *14*, 300−305.

(3) Li, S.; Zhan, L.; Yao, N.; Xia, X.; Chen, Z.; Yang, W.; He, C.; Zuo, L.; Shi, M.; Zhu, H.; Lu, X.; Zhang, F.; Chen, H. Unveiling

structure-performance relationships from multi-scales in non-fullerene organic photovoltaics. *Nat. Commun.* **2021**, *12*, 4627.
(4) Wei, Y.; Yu, J.; Qin, L.; Chen, H.; Wu, X.; Wei, Z.; Zhang, X.; Xiao, Z.; Ding, L.; Gao, F.; Huang, H. A universal method for constructing high efficiency organic solar cells with stacked structures. *Energy Environ. Sci.* **2021**, *14*, 2314−2321.
(5) Zheng, Z.; Wang, J.; Bi, P.; Ren, J.; Wang, Y.; Yang, Y.; Liu, X.; Zhang, S.; Hou, J. Tandem Organic Solar Cell with 20.2% Efficiency. *Joule* **2022**, *6*, 171−184.
(6) Zhan, L.; Li, S.; Li, Y.; Sun, R.; Min, J.; Bi, Z.; Ma, W.; Chen, Z.; Zhou, G.; Zhu, H.; Shi, M.; Zuo, L.; Chen, H. Desired open-circuit voltage increase enables efficiencies approaching 19% in symmetric-asymmetric molecule ternary organic photovoltaics. *Joule* **2022**, *6*, 662−675.
(7) Zuo, L.; Jo, S. B.; Li, Y.; Meng, Y.; Stoddard, R. J.; Liu, Y.; Lin, F.; Shi, X.; Liu, F.; Hillhouse, H. W.; Ginger, D. S.; Chen, H.; Jen, A. K.-Y. Dilution effect for highly efficient multiple-component organic solar cells. *Nat. Nanotechnol.* **2022**, *17*, 53−60.
(8) Li, C.; Zhou, J.; Song, J.; Xu, J.; Zhang, H.; Zhang, X.; Guo, J.; Zhu, L.; Wei, D.; Han, G.; Min, J.; Zhang, Y.; Xie, Z.; Yi, Y.; Yan, H.; Gao, F.; Liu, F.; Sun, Y. Non-fullerene acceptors with branched side chains and improved molecular packing to exceed 18% efficiency in organic solar cells. *Nat. Energy* **2021**, *6*, 605−613.
(9) Zhan, L.; Li, S.; Li, Y.; Sun, R.; Min, J.; Chen, Y.; Fang, J.; Ma, C.-Q.; Zhou, G.; Zhu, H.; Zuo, L.; Qiu, H.; Yin, S.; Chen, H. Manipulating Charge Transfer and Transport via Intermediary Electron Acceptor Channels Enables 19.3% Efficiency Organic Photovoltaics. *Adv. Energy Mater.* **2022**, *12*, No. 2201076.
(10) Wang, L.; An, Q.; Yan, L.; Bai, H.-R.; Jiang, M.; Mahmood, A.; Yang, C.; Zhi, H.; Wang, J.-L. Non-fullerene acceptors with hetero-dihalogenated terminals induce significant difference in single crystallography and enable binary organic solar cells with 17.5% efficiency. *Energy Environ. Sci.* **2022**, *15*, 320−333.
(11) Zhong, Z.; Chen, S.; Zhao, J.; Xie, J.; Zhang, K.; Jia, T.; Zhu, C.; Jing, J.; Liang, Y.; Hong, L.; Zhu, S.; Ma, D.; Huang, F. Non-Halogen Solvent Processed Binary Organic Solar Cells with Efficiency of 19% and Module Efficiency Over 15% Enabled by Asymmetric Alkyl Chain Engineering. *Adv. Energy Mater.* **2023**, *13*, No. 2302273.
(12) Liu, F.; Jiang, Y.; Xu, R.; Su, W.; Wang, S.; Zhang, Y.; Liu, K.; Xu, S.; Zhang, W.; Yi, Y.; Ma, W.; Zhu, X. Nonfullerene Acceptor Featuring Unique Self-Regulation Effect for Organic Solar Cells with 19% Efficiency. *Angew. Chem., Int. Ed.* **2024**, *63*, No. e202313791.
(13) Aldrich, T. J.; Matta, M.; Zhu, W.; Swick, S. M.; Stern, C. L.; Schatz, G. C.; Facchetti, A.; Melkonyan, F. S.; Marks, T. J. Fluorination effects on indacenodithienothiophene acceptor packing and electronic structure, end-group redistribution, and solar cell photovoltaic response. *J. Am. Chem. Soc.* **2019**, *141*, 3274−3287.
(14) Wei, Q.; Liu, W.; Leclerc, M.; Yuan, J.; Chen, H.; Zou, Y. A-DA'DA non-fullerene acceptors for high-performance organic solar cells. *Sci. China Chem.* **2020**, *63*, 1352−1366.
(15) Lai, H.; Zhao, Q.; Chen, Z.; Chen, H.; Chao, P.; Zhu, Y.; Lang, Y.; Zhen, N.; Mo, D.; Zhang, Y.; et al. Trifluoromethylation enables a 3D interpenetrated low-band-gap acceptor for efficient organic solar cells. *Joule* **2020**, *4*, 688−700.
(16) Kupgan, G.; Chen, X.; Brédas, J. Molecular packing of non-fullerene acceptors for organic solar cells: Distinctive local morphology in Y6 vs. *ITIC derivatives. Mater. Today Adv.* **2021**, *11*, No. 100154.
(17) Xiang, Y.; Cao, Z.; Zhang, X.; Zou, Z.; Zheng, S. Enhanced Photovoltaic Properties of Y6 Derivatives with Asymmetric Terminal Groups: A Theoretical Insight. *Int. J. Mol. Sci.* **2023**, *24*, 14753.
(18) Mahajan, C. L.; Gomez, E. D.; Milner, S. T. Resolving the Atomistic Morphology of Domains and Interfaces in PM6:Y6 with Molecular Dynamics. *Macromolecules* **2025**, *58*, 2765−2778.
(19) Huang, Y.; Yu, Z.; Yin, A.; Han, G.; Lang, X.; Brédas, J.; Wang, T.; Jiang, Q. Examining the Impact of 3D Multi-Arm Small Molecules on PM6:Y6 Blend Reveals the Key Requirements for Their Electronic Properties. *Angew. Chem., Int. Ed.* **2025**, *64*, No. e202418225.
(20) Zhang, Y.; Liu, Z.; Shan, T.; Wang, Y.; Zhu, L.; Li, T.; Liu, F.; Zhong, H. Tuning the molecular geometry and packing mode of non-fullerene acceptors by altering the bridge atoms towards efficient organic solar cells. *Mater. Chem. Front.* **2020**, *4*, 2462−2471.
(21) He, Q.; Ufimkin, P.; Aniés, F.; Hu, X.; Kafourou, P.; Rimmele, M.; Rapley, C. L.; Ding, B. Molecular engineering of Y-series acceptors for nonfullerene organic solar cells. *SusMat* **2022**, *2*, 591−606.
(22) Bai, Y.; Hong, L.; Dou, Y.; Zhu, S.; Tang, H.; Liu, D.; Cao, Y.; Chen, J.; Chen, S.; Shao, L.; Hu, Z.; Tang, D.; Zhang, K.; Su, S.-J.; Liu, C.; Huang, F. C-Shape or S-Shape? The Molecular Geometry Control of Fused-Ring Nonfullerene Acceptors for Lower Energy Loss in Organic Solar Cells. *ACS Energy Lett.* **2024**, *9*, 1786−1795.
(23) Sewak, R.; Khatua, R.; Mondal, A. Non-covalent interactions in conjugated polymer blends: Insights into the stability of PVC/PM6 and CPE/PM6 systems. *J. Chem. Phys.* **2024**, *161*, 214902.
(24) Schmidle, H.; Hall, C. K.; Velev, O. D.; Klapp, S. H. L. Phase diagram of two-dimensional systems of dipole-like colloids. *Soft Matter* **2012**, *8*, 1521−1531.
(25) Gartner, T. E., III; Jayaraman, A. Modeling and Simulations of Polymers: A Roadmap. *Macromolecules* **2019**, *52*, 755−786.
(26) Nielsen, A.; Holder, A. *Gauss View 5.0, User's Reference*; Gaussian Inc.: Pittsburgh, 2009.
(27) Frisch, M. J.; Trucks, G. W.; Schlegel, H. B.; Scuseria, G. E.; Robb, M. A.; Cheeseman, J. R.; Scalmani, G.; Barone, V.; Mennucci, B.; Petersson, G. A.; Nakatsuji, H.; Caricato, M.; Li, X.; Hratchian, H. P.; Izmaylov, A. F.; Bloino, J.; Zheng, G.; Sonnenberg, J. L.; Hada, M.; Ehara, M.; Toyota, K.; Fukuda, R.; Hasegawa, J.; Ishida, M.; Nakajima, T.; Honda, Y.; Kitao, O.; Nakai, H.; Vreven, T.; Montgomery, J. A. Jr.; Peralta, J. E.; Ogliaro, F.; Bearpark, M.; Heyd, J. J.; Brothers, E.; Kudin, K. N.; Staroverov, V. N.; Kobayashi, R.; Normand, J.; Raghavachari, K.; Rendell, A.; Burant, J. C.; Iyengar, S. S.; Tomasi, J.; Cossi, M.; Rega, N.; Millam, J. M.; Klene, M.; Knox, J. E.; Cross, J. B.; Bakken, V.; Adamo, C.; Jaramillo, J.; Gomperts, R.; Stratmann, R. E.; Yazyev, O.; Austin, A. J.; Cammi, R.; Pomelli, C.; Ochterski, J. W.; Martin, R. L.; Morokuma, K.; Zakrzewski, V. G.; Voth, G. A.; Salvador, P.; Dannenberg, J. J.; Dapprich, S.; Daniels, A. D.; Farkas, Ö.; Foresman, J. B.; Ortiz, J. V.; Cioslowski, J.; Fox, D. J. *Gaussian 09 Revision E.01*; Gaussian Inc.: Wallingford CT, 2009.
(28) Abraham, M. J.; Murtola, T.; Schulz, R.; Páll, S.; Smith, J. C.; Hess, B.; Lindahl, E. GROMACS: High performance molecular simulations through multi-level parallelism from laptops to supercomputers. *SoftwareX* **2015**, *1−2*, 19−25.
(29) Hess, B.; Kutzner, C.; Van Der Spoel, D.; Lindahl, E. GROMACS 4: Algorithms for Highly Efficient, Load-Balanced, and Scalable Molecular Simulation. *J. Chem. Theory Comput.* **2008**, *4*, 435−447.
(30) Lu, T. *Sobtop, Version [dev3.1]*, 2024. http://sobereva.com/soft/Sobtop/, (accessed: November 2024).
(31) Tang, X.; Jiang, B.; Gong, Y.; Jin, Y.; He, J.; Xie, H.; Guo, S.; Liu, Y. Designing Nonconventional Luminescent Materials with Efficient Emission in Dilute Solutions via Modulation of Dynamic Hydrogen Bonds. *Molecules* **2023**, *28*, 5240.
(32) Yu, H.; Wang, Y.; Kwok, C. H.; Zhou, R.; Yao, Z.; Mukherjee, S.; Sergeev, A.; Hu, H.; Fu, Y.; Ng, H. M.; Chen, L.; Zhang, D.; Zhao, D.; Zheng, Z.; Lu, X.; Yin, H.; Wong, K. S.; Ade, H.; Zhang, C.; Zhu, Z.; Yan, H. A polymer acceptor with double-decker configuration enhances molecular packing for high-performance all-polymer solar cells. *Joule* **2024**, *8*, 2304−2324.
(33) Lu, T. A comprehensive electron wavefunction analysis toolbox for chemists, Multiwfn. *J. Chem. Phys.* **2024**, *161*, No. 082503.
(34) Bussi, G.; Donadio, D.; Parrinello, M. Canonical sampling through velocity rescaling. *J. Chem. Phys.* **2007**, *126*, No. 014101.
(35) Berendsen, H. J. C.; Postma, J. P. M.; van Gunsteren, W. F.; DiNola, A.; Haak, J. R. Molecular dynamics with coupling to an external bath. *J. Chem. Phys.* **1984**, *81*, 3684−3690.
(36) Gunsteren, W. F. V.; Berendsen, H. J. C. A Leap-frog Algorithm for Stochastic Dynamics. *Mol. Simul.* **1988**, *1*, 173−185.

https://doi.org/10.1021/acsaem.5c01643
ACS Appl. Energy Mater. XXXX, XXX, XXX−XXX

(37) Kotadiya, N. B.; Lu, H.; Mondal, A.; Ie, Y.; Andrienko, D.; Blom, P. W. M.; Wetzelaer, G.-J. A. H. Universal strategy for Ohmic hole injection into organic semiconductors with high ionization energies. *Nat. Mater.* **2018**, *17*, 329−334.
(38) Mondal, A.; Paterson, L.; Cho, J.; Lin, K. H.; van der Zee, B.; Wetzelaer, G. J. A. H.; Stankevych, A.; Vakhnin, A.; Kim, J. J.; Kadashchuk, A.; Blom, P. W. M.; May, F.; Andrienko, D. Molecular library of OLED host materials—Evaluating the multiscale simulation workflow. *Chem. Phys. Rev.* **2021**, *2*, No. 031304.
(39) Humphrey, W.; Dalke, A.; Schulten, K. VMD: Visual molecular dynamics. *J. Mol. Graph.* **1996**, *14*, 33−38.
(40) Brehm, M.; Kirchner, B. TRAVIS - A Free Analyzer and Visualizer for Monte Carlo and Molecular Dynamics Trajectories. *J. Chem. Inf. Model.* **2011**, *51*, 2007−2023.
(41) Brehm, M.; Thomas, M.; Gehrke, S.; Kirchner, B. TRAVIS—A free analyzer for trajectories from molecular simulation. *J. Chem. Phys.* **2020**, *152*, 164105.
(42) Boto, R. A.; Peccati, F.; Laplaza, R.; Quan, C.; Carbone, A.; Piquemal, J.-P.; Maday, Y.; Contreras-Garcí'a, J. NCIPLOT4: Fast, Robust, and Quantitative Analysis of Noncovalent Interactions. *J. Chem. Theory Comput.* **2020**, *16*, 4150−4158.
(43) Na, S.; Xumin, L.; Yong, G.Research on k-means Clustering Algorithm: An Improved k-means Clustering Algorithm. *Third International Symposium on Intelligent Information Technology and Security Informatics*; IEEE: Jian, China, 2010, *2010*, 63−67.
(44) Pedregosa, F.; Varoquaux, G.; Gramfort, A.; Michel, V.; Thirion, B.; Grisel, O.; Blondel, M.; Prettenhofer, P.; Weiss, R.; Dubourg, V.; Vanderplas, J.; Passos, A.; Cournapeau, D.; Brucher, M.; Perrot, M.; Duchesnay, E. Scikit-learn: Machine learning in Python. *J. Mach. Learn. Res.* **2011**, *12*, 2825−2830.
(45) Lazar, E. A.; Lu, J.; Rycroft, C. H. Voronoi cell analysis: The shapes of particle systems. *Am. J. Phys.* **2022**, *90*, 469−480.
(46) Weis, S.; Schröter, M. Analyzing X-ray tomographies of granular packings. *Rev. Sci. Instrum.* **2017**, *88*, No. 051809.
(47) Stukowski, A. Visualization and analysis of atomistic simulation data with OVITO−the Open Visualization Tool. *Model. Simul. Mater. Sci. Eng.* **2010**, *18*, No. 015012.
(48) Lu, T.; Chen, Q. Simple, Efficient, and Universal Energy Decomposition Analysis Method Based on Dispersion-Corrected Density Functional Theory. *J. Phys. Chem. A* **2023**, *127*, 7023−7035.
(49) Heßelmann, A.; Jansen, G. The helium dimer potential from a combined density functional theory and symmetry-adapted perturbation theory approach using an exact exchange−correlation potential. *Phys. Chem. Chem. Phys.* **2003**, *5*, 5010−5014.
(50) Heßelmann, A.; Jansen, G. Intermolecular dispersion energies from time-dependent density functional theory. *Chem. Phys. Lett.* **2003**, *367*, 778−784.
(51) Balci, K.; Akkaya, Y.; Akyuz, S. An experimental and theoretical vibrational spectroscopic study on niflumic acid, a non-steroidal anti-inflammatory drug. *Vib. Spectrosc.* **2010**, *53*, 239−247.
(52) Contreras-García, J.; Johnson, E. R.; Keinan, S.; Chaudret, R.; Piquemal, J.-P.; Beratan, D. N.; Yang, W. NCIPLOT: A Program for Plotting Noncovalent Interaction Regions. *J. Chem. Theory Comput.* **2011**, *7*, 625−632.
(53) Johnson, E. R.; Keinan, S.; Mori-Sánchez, P.; Contreras-García, J.; Cohen, A. J.; Yang, W. Revealing Noncovalent Interactions. *J. Am. Chem. Soc.* **2010**, *132*, 6498−6506.
(54) Venkataramanan, N. S.; Suvitha, A.; Kawazoe, Y. Intermolecular interaction in nucleobases and dimethyl sulfoxide/water molecules: A DFT, NBO, AIM and NCI analysis. *J. Mol. Graphics Modell.* **2017**, *78*, 48−60.
(55) Wieduwilt, E. K.; Boto, R. A.; Macetti, G.; Laplaza, R.; Contreras-García, J.; Genoni, A. Extracting Quantitative Information at Quantum Mechanical Level from Noncovalent Interaction Index Analyses. *J. Chem. Theory Comput.* **2023**, *19*, 1063−1079.
(56) Yuan, J.; Zhang, Y.; Zhou, L.; Zhang, G.; Yip, H.-L.; Lau, T.-K.; Lu, X.; Zhu, C.; Peng, H.; Johnson, P. A.; Leclerc, M.; Cao, Y.; Ulanski, J.; Li, Y.; Zou, Y. Single-Junction Organic Solar Cell with over 15% Efficiency Using Fused-Ring Acceptor with Electron-Deficient Core. *Joule* **2019**, *3*, 1140−1151.
(57) Caliński, T.; Harabasz, J. A dendrite method for cluster analysis. *Commun. Stat.* **1974**, *3*, 1−27.
(58) Levet, F. Optimizing Voronoi-based quantifications for reaching interactive analysis of 3D localizations in the million range. *Front. Bioinform.* **2023**, *3*, No. 1249291.
(59) Woolhouse, F.; Dierking, I. Thin Cells of Polymer-Modified Liquid Crystals Described by Voronoi Diagrams. *Materials* **2025**, *18*, 1106.
(60) Tomić, N. Z.; Milanović, P.; Meo, B.; Vuksanović, M. M.; Veljović; Rakin, M.; Heinemann, R. J. Image analysis and the finite element method in the characterization of the influence of porosity parameters on the mechanical properties of porous EVA/PMMA polymer blends. *Mech. Mater.* **2019**, *129*, 1−14.
(61) Deokar, R.; Banpurkar, A. G.; Singh, A. R.; Mehta, J.; Gajengi, A.; Thatai, S.; Pahwa, N.; Nalawade, S. Morphological, Optical and Voronoi Polygon Analysis of Breath Figures Prepared on Polymeric Surface. *Indian J. Sci. Technol.* **2024**, *17*, 1180−1188.
(62) Ahmadi, H.; van Heugten, P. M. H.; Veber, A.; Puskar, L.; Anderson, P. D.; Cardinaels, R. Toughening Immiscible Polymer Blends: The Role of Interface-Crystallization-Induced Compatibilization Explored Through Nanoscale Visualization. *ACS Appl. Mater. Interfaces* **2024**, *16*, 59174−59187.
(63) Ren, J.; Bao, X.; Han, L.; Wang, J.; Qiu, M.; Zhu, Q.; Hu, T.; Sheng, R.; Sun, M.; Yang, R. 4,7-Di-2-thienyl-2,1,3-benzothiadiazole with hexylthiophene side chains and a benzodithiophene based copolymer for efficient organic solar cells. *Polym. Chem.* **2015**, *6*, 4415−4423.
(64) Ye, L.; Weng, K.; Xu, J.; Du, X.; Chandrabose, S.; Chen, K.; Zhou, J.; Han, G.; Tan, S.; Xie, Z.; Yi, Y.; Li, N.; Liu, F.; Hodgkiss, J. M.; Brabec, C. J.; Sun, Y. Unraveling the influence of non-fullerene acceptor molecular packing on photovoltaic performance of organic solar cells. *Nat. Commun.* **2020**, *11*, 6005.

https://doi.org/10.1021/acsaem.5c01643
ACS Appl. Energy Mater. XXXX, XXX, XXX−XXX